OPEN ACCESS
JOURNAL OF ADVANCED DIELECTRICS
Vol. 13, No. 1 (2023) 2242001 (7 pages)

DOI: 10.1142/S2010135X22420012

Superior energy storage efficiency through tailoring relaxor behavior and band energy gap in KNN-based ferroelectric ceramic capacitors

Limin Hou*, Changxiao Li*, Xinjian Wang*, Xiaozhi Wang†, Ting Wang‡ and Yu Huan*,§

*School of Materials Science and Engineering, University of Jinan, Jinan 250022, P. R. China

†Electronic Materials Research Laboratory, Key Laboratory of the Ministry of Education and International Center for Dielectric Research, Xi'an Jiaotong University, Xi'an 710032, P. R. China

‡Guangdong Provincial Key Laboratory of Electronic Functional Materials and Devices Huizhou University, Huizhou, Guangdong, 516001, P. R. China

§mse_huany@ujn.edu.cn

Received 8 May 2022; Revised 14 June 2022; Accepted 4 July 2022; Published 28 September 2022

With the increasing demand of high-power and pulsed power electronic devices, environmental-friendly potassium sodium niobate ($(Na_{0.5}K_{0.5})NbO_3$, KNN) ceramic-based capacitors have attracted much attention in recent years owning to the boosted energy storage density (W_{rec}). Nevertheless, the dielectric loss also increases as the external electric field increases, which will generate much dissipated energy and raise the temperature of ceramic capacitors. Thus, an effective strategy is proposed to enhance the energy storage efficiency (η) via tailoring relaxor behavior and bad gap energy in the ferroelectric $0.9(Na_{0.5}K_{0.5})$-NbO_3–$0.1Bi(Zn_{2/3}(Nb_xTa_{1-x})_{1/3})O_3$ ceramics. On the one hand, the more diverse ions in the B-sites owing to introducing the Ta could further disturb the long-range ferroelectric polar order to form the short–range polar nanoregions (PNRs), resulting in the high η. On the other hand, the introduction of Ta ions could boost the intrinsic band energy gap and thus improve the E_b. As a result, high W_{rec} of 3.29 J/cm^3 and ultrahigh η of 90.1% at the high external electric field of 310 kV/cm are achieved in $x = 0.5$ sample. These results reveal that the KNN-based ceramics are promising lead-free candidate for high-power electronic devices.

Keywords: Lead-free dielectric ceramic capacitor; KNN-based ceramics; energy storage efficiency; band gap energy; relaxor behavior.

1. Introduction

Energy storage technologies and corresponding materials have attracted much attention in recent years due to the energy crisis and environment problems.[1,2] Compared with the common batteries, fuel cells and supercapacitors, the dielectric ceramic capacitors exhibited high-power density (~10^8 W/kg), fast charging–discharging rate (~ns), and high operating temperature (>200°C), which have great potential for high-power or pulsed power systems.[3–6] However, their energy storage density could not be comparable to these chemical storage devices, which severe restricts their practical application and industrial development.[7] As an electrostatic energy storage, whose energy storage density and efficiency of the dielectric ceramic capacitors can be calculated by polarization-electric field (P–E) hysteresis curves, as shown in Fig. 1. The total charged energy storage density (W) is determined by the area between the y-axis and the charge polarization curve, while the recoverable energy storage density (W_{rec}) is calculated by the area between the y-axis and the discharge polarization curve, according to the following equations[8,9]:

$$W = \int_0^{P_{max}} E\mathrm{d}P, \tag{1}$$

$$W_{rec} = \int_{P_r}^{P_{max}} E\mathrm{d}P, \tag{2}$$

where E is applied electric field, P is the polarization intensity, P_{max}, and P_r represent the maximum and remnant polarization, respectively. W–W_{rec} is the dissipated energy. The dissipated energy would be transformed into heat. It would raise the temperature of dielectric capacitor and increase the risk of electrical breakdown.[10] Therefore, the lower the dissipated energy, the better for the practical application. The dissipated energy could be assessed by the energy storage efficiency (η), which is expressed by the following formula:

$$\eta = \frac{W_{rec}}{W} \times 100\%. \tag{3}$$

The low dissipated energy means the high η. Considering that the large breakdown electric field (E_b) is necessary for

§Corresponding author.

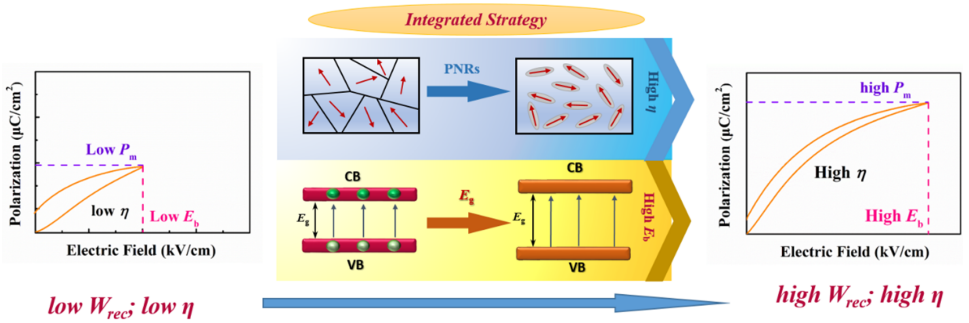

Fig. 1. Schematic diagram of optimization strategy in this work.

the high W_{rec}, the construction of novel dielectric ceramic capacitors with ultrahigh η at high electric field becomes the urgent issues at present.

Among the most investigated dielectric ceramic materials, the linear dielectrics and relaxor ferroelectrics usually exhibited higher η compared with the antiferroelectrics.[11–13] The first-order induced-field phase transitions in antiferroelectrics could greatly reduce the η and increase the heat loss.[14] Nevertheless, the ultralow polarization of linear dielectrics (such as $SrTiO_3$, $CaTiO_3$) severely limits the enhancement of W_{rec}.[15] As a result, the lead-free relaxor ferroelectrics (such as $(Bi_{0.5}Na_{0.5})TiO_3$, $BaTiO_3$ and $(K_{0.5}Na_{0.5})NbO_3$) become one of the most promising ceramic capacitors in order to protect the human health and environment.[16,17] In recent years, the $K_{0.5}Na_{0.5}NbO_3$ (KNN)-based relaxor ferroelectrics attracted much attention owing to the boosted E_b. For instance, Du *et al.* boosted the E_b from ~200 kV/cm to ~870 kV/cm by tailoring the doping component $Bi(Ni_{0.5}Zr_{0.5})O_3$ in KNN ceramics.[18] However, the η is lower than 90%. The common process to enhance the η is to construct the short-range ordered polar nanoregions (PNRs), which could quickly response to the external electric field.[19] Additionally, the aligned PNRs along the external electric field direction will rapidly recover to the original disorder state, thus generating the small P_r and high η once the external electric field is removed.[20] Many researchers verified that doping the appropriate secondary solid solution in the ferroelectrics can effectively reduce the ferroelectric order size.[21]

In this work, an integrated strategy to improve η under the high electric field is proposed, as sketched in Fig. 1. The perovskite oxide $Bi(Zn_{2/3}(Nb_xTa_{1-x})_{1/3})O_3$ is introduced into $(Na_{0.5}K_{0.5})NbO_3$ matrix to form binary solid solution ceramics $0.9(Na_{0.5}K_{0.5})NbO_3$–$0.1Bi(Zn_{2/3}(Nb_xTa_{1-x})_{1/3})O_3$ ($0.9KNN–0.1BZT_xN_{(1-x)}$, x = 0, 0.25, 0.5, 0.75, 1) ferroelectric ceramics based on following consideration. On the one hand, the more diverse ions in the B-sites owing to introducing the Ta could further disturb the long-range ferroelectric polar order to form the short-range PNRs, i.e., enhance the dielectric relaxor behavior, which would result the small P_r and high η. On the other hand, the introduction of Ta ions could boost the intrinsic band energy gap and thus improve the E_b. As a result, high W_{rec} of 3.29 J/cm^3 and ultrahigh η of 90.1% at the high external electric field of 310 kV/cm were achieved in x = 0.5 sample. These results reveal that the KNN-based ceramics are promising lead-free candidate for high-power electronic devices.

2. Experimental Section

A series of $0.9KNN–0.1BZT_xN_{(1-x)}$ were fabricated by conventional solid state reaction method using the oxides and carbonate of K_2CO_3 (99.9%), Na_2CO_3 (99.9%), Nb_2O_5 (99.99%), Bi_2O_3 (99.9%), ZnO (99.9%), Ta_2O_5 (99.5%). All the raw materials were purchased from Shanghai Macklin Biochemical Co. Ltd. First, the raw materials were dried to remove the absorbed water, weighted according to the designed stoichiometric formula, and then ball-milled with ethanol and ZrO_2 ball for 12 h in a planetary ball mill. Next, the mixed chemicals were dried to remove ethanol and subsequently were calcined twice at 800°C for 3 h in alumina crucibles. Subsequently, the calcined powders were ball-milled again for 12 h. After drying, the mixed powders were pressed into disks with polyvinyl butyral (PVB) as binder. The diameter and thickness of the green disks were about 10 mm and 0.8 mm, respectively. Finally, the disks were sintered at 1090–1120°C for 3 h according to their composition. Before electrical measurement, the ceramics were polished to about 0.05 mm with Au electrode with the diameter of ~3 mm.

The crystalline structure of $0.9KNN–0.1BZT_xN_{(1-x)}$ ceramics was analyzed by X-ray diffraction (XRD, SmartLab, Rigaku, Tokyo, Japan) with Cu K_α radiation (λ = 0.15406 nm). The surface microstructure of as-sintered ceramics was measured by the field-emission scanning electron microscopy (SEM, LEO-1530, OberkoChen, Germany). The transmission electron microscopy (TEM, JEOL2100, Japan) was carried out to observe the microstructure of the sample. The band-gap energy of the ceramics was measured using an ultraviolet–visible (UV–Vis) spectrophotometer (UV–2550; Shimadzu, Tokyo, Japan). The temperature-dependent dielectric properties were determined by the LCR meter (Keysight E4980, Santa Rosa, CA). The polarization versus electric field hysteresis (P–E) curves were measured by a ferroelectric analyzer

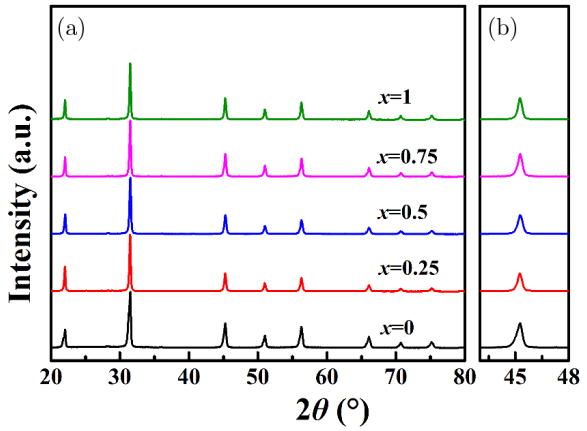

Fig. 2. (a) XRD patterns of 0.9KNN–0.1BZT$_x$N$_{(1-x)}$ ceramics at room temperature. (b) Enlarged XRD patterns in the 2θ range of 43.5–48°.

(Radiant Technologies Inc., USA). The charge–discharge properties were conducted by a commercial charge–discharge platform (PK-CPR1701, PolyK Technologies, PA, USA).

3. Results and Discussion

Figure 2(a) depicts the room temperature XRD patterns of 0.9KNN–0.1BZT$_x$N$_{(1-x)}$ ceramics. All the samples exhibit a pure perovskite structure without any secondary phase, indicating the sintered ceramics could well form solid solutions because the tolerance factor of the doping BZT$_x$N$_{(1-x)}$ (~0.93) is similar to that of KNN matrix (~0.94). The enlarged (200) diffraction peak in the 2θ range of 43.5–48° for all composition is shown in Fig. 2(b). It can be obviously observed that all the (200) diffraction peaks are unimodal with symmetrical structure for all the compositions, suggesting all the ceramics are dominated by pseudocubic phase structure. The approximate symmetrical phase structure is beneficial to facilitate the energy storage performance.[22] In addition, all the peaks locate the nearly same angle, owing to the almost the same ion radius of Ta^{5+} (R_{Ta}^{5+} = 0.64, CN = 6) and Nb^{5+} (R_{Nb}^{5+} = 0.64, CN = 6).[23]

Temperature-dependent dielectric constant (ε_r) and loss (tanδ) of all ceramics are shown in Figs. 3(a)–3(e). At room temperature, the tanδ of all the ceramics exhibits the value lower than 0.15 over all the testing frequencies. Meanwhile, the tanδ of all ceramics keeps a low value at a wide temperature range from room temperature to 300°C, which demonstrates that the excellent insulating properties. The low tanδ is beneficial to reduce the dissipated energy and thus improve the E_b.[24,25] Only one dielectric anomaly featuring can be seen, which should be ascribed to the ferroelectric–paraelectric phase transition. Additionally, the dielectric anomaly featuring of all the ceramic locates at the almost same temperature (room temperature to 100°C). The results coincide well with the XRD patterns. The dielectric peaks are very broad and flattened, which indicates the thermal stability in dielectric behavior of the ceramic samples. The temperature corresponding to the maximum dielectric constant (ε_m), i.e., T_m, increases with increasing frequencies. The two characteristics are the typical feature of the relaxor ferroelectrics.[26] To assess the relaxor behavior, the diffusion coefficient (γ) is fitted by the modified Curie–Weiss equation[27]:

$$1/\varepsilon_r - 1/\varepsilon_m = (T - T_m)^\gamma / C, \quad (4)$$

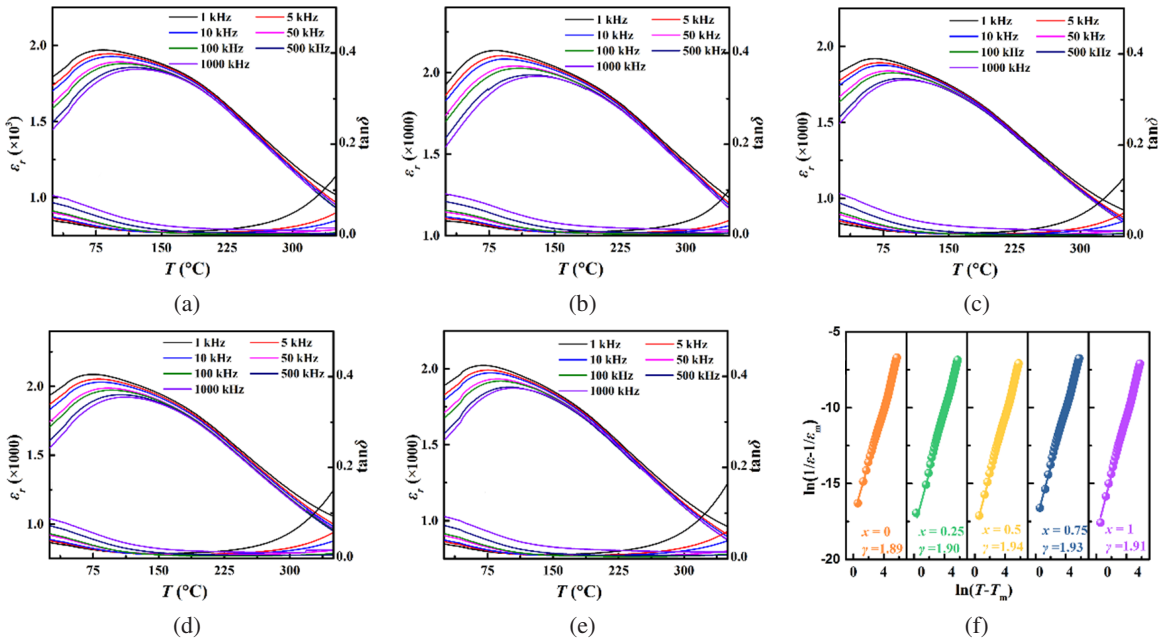

Fig. 3. Temperature-dependent ε_r and tanδ of 0.9KNN–0.1BZT$_x$N$_{(1-x)}$ ceramics at various frequencies: (a) x = 0, (b) x = 0.25, (c) x = 0.5, (d) x = 0.75, (e) x = 1. (f) Plots of ln(1/ε_r–1/ε_m) versus ln(T–T_m) and relaxor coefficient.

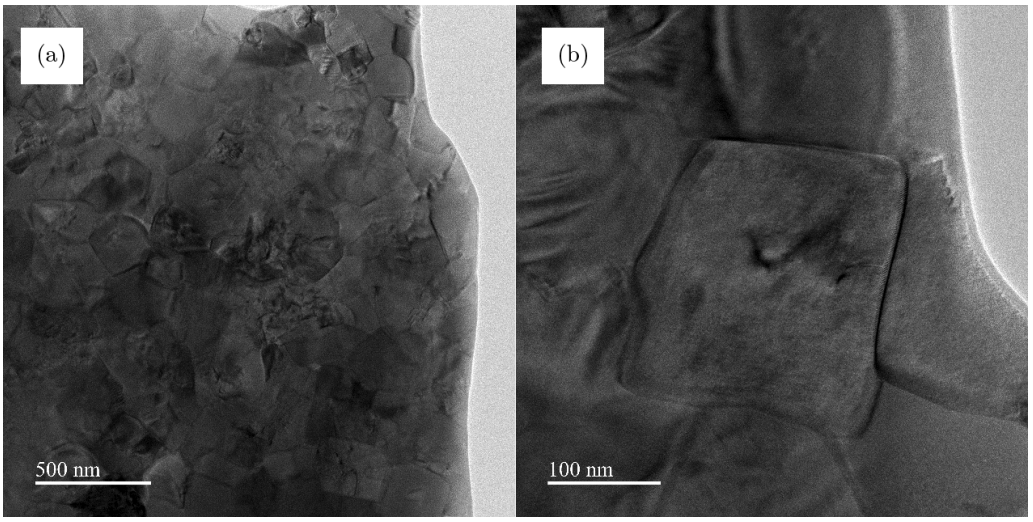

Fig. 4. TEM image of $x = 0.5$ sample.

where C is Curie constant. The $\ln(1/\varepsilon_r - 1/\varepsilon_m)$ versus $\ln(T - T_m)$ curves and relaxor coefficient are plotted in Fig. 3(f). The γ value first increases and then decreases, achieving the maximum when $x = 0.5$. It demonstrates that the $x = 0.5$ sample exhibited the distinct relaxor behavior, which should be correlated with the more complicated ion species in B-site on account of the replacement of Nb^{5+} by Ta^{5+}. The enhanced relaxor behavior could improve the energy storage efficiency of the dielectric ceramics.

The relaxor behavior is again confirmed by TEM analysis. TEM image of x = 0.5 sample is displayed in Fig. 4. The submicron grains are closely arranged without any pores, as displayed in Fig. 4(a), demonstrating the compact morphology of the ceramics. The typical stripped domains of KNN-based ceramics are not found in the grains.[28] Whereas, the featureless PNRs could be obviously observed in the TEM bright-field image in Fig. 4(b),[29] which is consistent with the relaxor behavior obtained by the temperature dependence of the dielectric properties in Fig. 3. The PNRs could quickly response to the external electric field, and recover to the original disorder state, consequently achieving the low P_r and high η.[30,31] The formation of PNRs is related to the random local electric and elastic field because Bi^{3+}, Na^+, K^+ occupied the A-sites, and Nb^{5+}, Zn^{2+}, Ta^{5+} occupied the B-site.[26] In addition, the grain size is submicron-scale and these grains are closely stacked without any pores, demonstrating the high compactness of the as-sintered ceramics. It is also confirmed

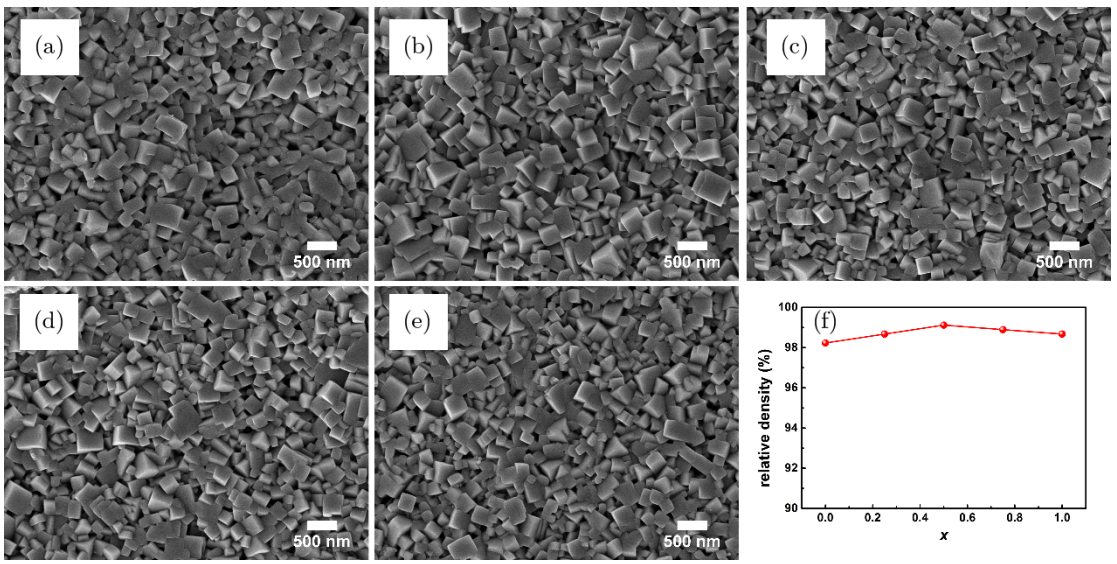

Fig. 5. Typical SEM morphologies of $0.9KNN–0.1BZT_xN_{(1-x)}$ ceramics: (a) $x = 0$, (b) $x = 0.25$, (c) $x = 0.5$, (d) $x = 0.75$, (e) $x = 1$. (f) Relative density of $0.9KNN–0.1BZT_xN_{(1-x)}$ ceramics.

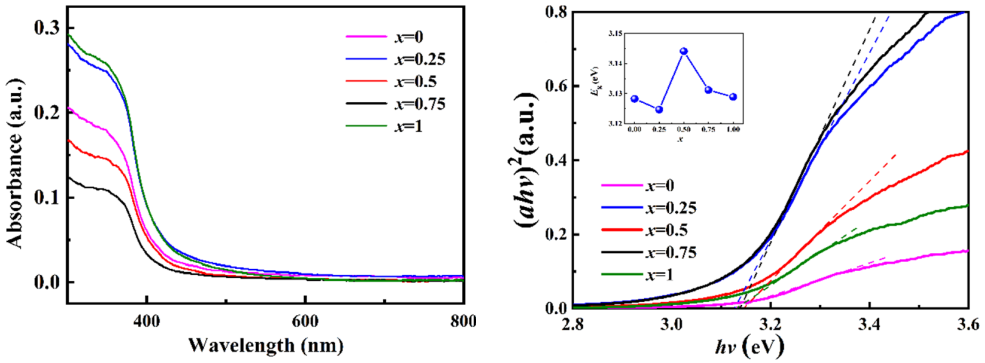

(a) (b)

Fig. 6. (a) UV–Visible absorbance spectra of 0.9KNN–0.1BZT$_x$N$_{(1-x)}$ ceramics. (b) Plots of $(\alpha h\nu)^2$ versus $h\nu$, and inset is the calculated E_g.

by the SEM morphologies in Fig. 5. All the ceramics exhibited a dense microstructure without any visible pores. The relative density of the ceramics is plotted in Fig. 5(f). It can be found that all the relative density values are higher than 98%. Besides, all the ceramics exhibit the similar small grain with the average grain size <200 nm. The fine grain and high compactness are beneficial to enhance the E_b. Especially, the highest relative density of $x = 0.5$ ceramic might generate the highest E_b.

The UV–Visible absorbance spectra of 0.9KNN–0.1BZT$_x$N$_{(1-x)}$ ceramics are carried out to investigate the influence of the Ta/Nb ions on the band-gap energy (E_g),as displayed in Fig. 6(a). The E_g values are calculated according to the following calculation formula:

$$(ah\nu)^2 = A(h\nu - E_g), \tag{5}$$

where h is Planck constant, α is absorption factor, A is a constant, and ν is photon frequency. $(\alpha h\nu)^2$ versus $h\nu$ curves are plotted in Fig. 6(b) and the evolution of E_g is depicted in the corresponding inset. Notably, the E_g value first increases and then decreases, achieving the maximum value (3.144 eV) when $x = 0.5$. The large E_g value means the high transition energy for the electrons from valence band (VB) to conduction band (CB). As a consequence, the $x = 0.5$ sample obtains the highest E_b because intrinsic E_b and E_g obey the following relationship[32]:

$$E_b = 1.36\times10^7 \times \left(\frac{E_g}{4.0}\right)^3 (\text{V cm}^{-1}). \tag{6}$$

Figure 7 displays room temperature unipolar P–E curves of the 0.9KNN–0.1BZT$_x$N$_{(1-x)}$ ceramics measured at various

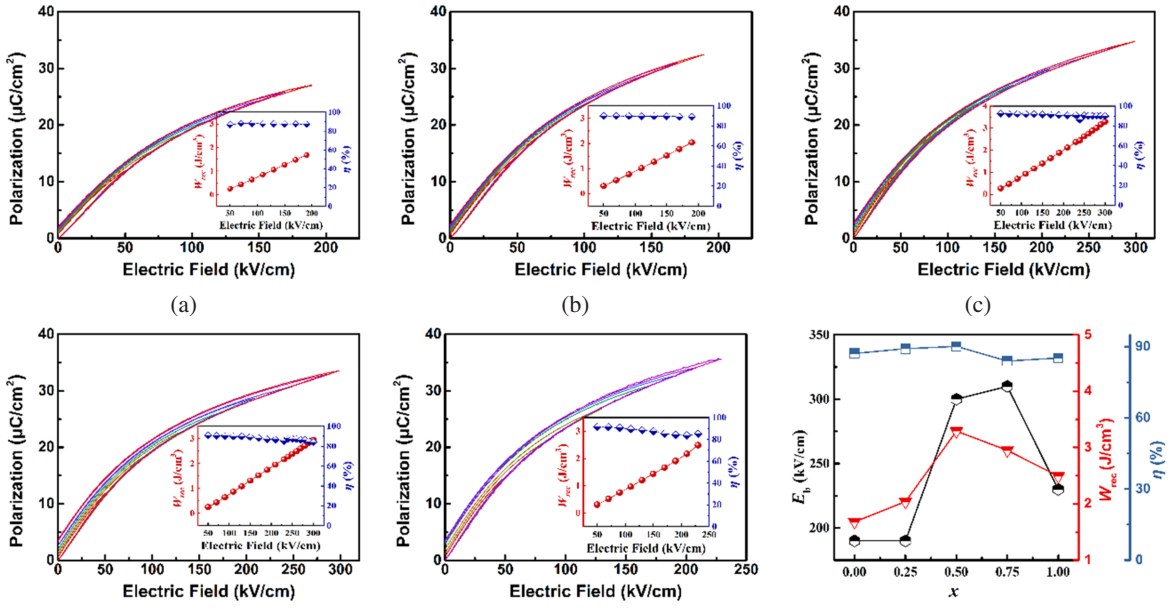

Fig. 7. Room temperature unipolar P–E curves of 0.9KNN–0.1BZT$_x$N$_{(1-x)}$ ceramics at different electric fields, and insets are the corresponding evolutions of W_{rec} and η values as function of electric field. (f) The evolutions of E_b, W_{rec} and η values as a function of x.

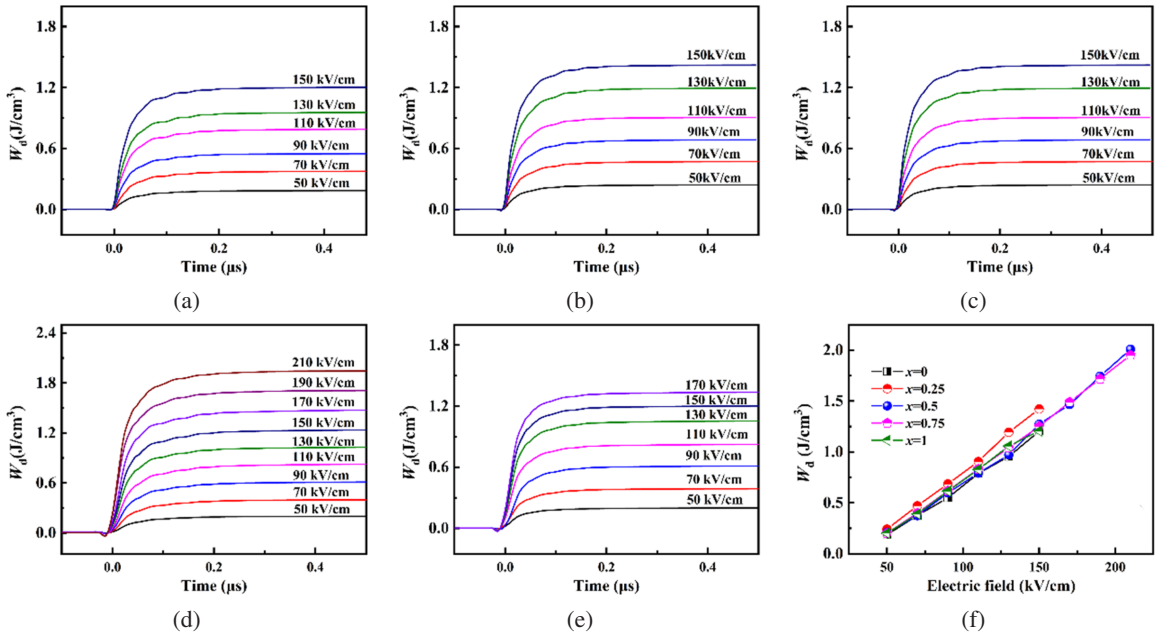

Fig. 8. The actual discharged energy density–time curves of 0.9KNN–0.1BZT$_x$N$_{(1-x)}$ ceramics at various electric fields. (f) The variations of W_d as a function of electric field.

external electric fields with a fixed frequency of 10 Hz. The W_{rec} and η as a function of external electric field are summarized in the corresponding insets. Furthermore, the evolutions of E_b, η, and W_{rec} as a function of x are plotted in Fig. 7(f). The maximum electric field, i.e., E_b, first increases and then decreases, achieving the peak value when $x = 0.5$ (190, 200, 310, 300, 230 kV/cm for $x = 0$, $x = 0.25$, $x = 0.5$, $x = 0.75$, $x = 1$ samples, respectively). The boosted electric breakdown strength is ascribed to the compact microstructure and enhanced band energy gap. The large E_b could rapidly boost the energy storage properties. It can be observed that W_{rec} linearly increases as the external electric field increases as shown in Figs. 7(a)–7(e). In addition, the η remains the high value until the ceramic is electrical breakdown. The high η is consistence with the slim profiles of the *P–E* curve, which results from the relaxor behavior of the ceramics. Especially, the $x = 0.5$ sample owns the high η of 90.1% at the high external electric field of 310 kV/cm, which is better than the other sample (87.13% at 190 kV/cm for $x = 0$, 89.134% at 200 kV/cm for $x = 0.25$, 83.94% at 300 kV/cm for $x = 0.75$, 85.19% at 230 kV/cm for $x = 1$) as summarized in Fig. 7(f). The high η at high electric field should be ascribed to the short-range PNRs, which could quickly response to the external electric field. The high η means the low dissipated energy and thus small (W–W_{rec}). The improved E_b and η generated the excellent W_{rec} (3.29 J/cm^3) for $x = 0.5$ sample, which is much better than the other samples (1.68 J/cm^3 at 190 kV/cm for $x = 0$, 2.04 J/cm^3 at 200 kV/cm for $x = 0.25$, 2.95 J/cm^3 at 300 kV/cm for $x = 0.75$, 2.49 J/cm^3 at 230 kV/cm for $x = 1$).

To evaluate the actual application performance, the overdamped discharged properties of the 0.9KNN–0.1BZT$_x$N$_{(1-x)}$ ceramics under different electric fields with a load resistor of 13 kΩ are measured. The actual discharged energy density (W_d) as a function of time is displayed in Fig. 8. The stored energy could be completed released in a very short time, indicating the great promising for pulsed power electronic devices. Figure 8(f) summarizes the variation of W_d as a function of electric field. The W_d of all the ceramics exhibits a linear increased tendency as the external electric field increases. The W_d value is smaller than the W_{rec} value for the same sample under the same electric field on account of the difference in measuring time between the *P–E* method and actual discharging method.[33,34] Nevertheless, W_d and W_{rec} show the similar variation rule. W_d achieved the maximum value of 2.01 J/cm^3 for $x = 0.5$ sample, which is higher than the other samples (1.23 J/cm^3 at 150 kV/cm for $x = 0$, 1.42 J/cm^3 at 150 kV/cm for $x = 0.25$, 1.95 J/cm^3 at 210 kV/cm for $x = 0.75$, 1.22 J/cm^3 at 150 kV/cm for $x = 1$). The high actual discharged energy density and fast discharged rate demonstrate that the as-prepared ceramics could be applied for pulsed power electronic devices.

4. Conclusions

The lead-free 0.9(Na$_{0.5}$K$_{0.5}$)NbO$_3$–0.1Bi(Zn$_{2/3}$(Nb$_x$Ta$_{1-x}$)$_{1/3}$)-O$_3$ relaxor ferroelectric ceramics are successfully synthesized and systematically investigated. All the ceramics exhibit the pure pseudocubic perovskite structure and compact microstructure. Moreover, the introduction of Ta ions could boost the intrinsic band energy gap and thus improve the transition energy for the electrons from VB to CB, which is responsible for enhanced E_b. In addition, the more diverse ions in the

B-sites owing to introducing the Ta could further disturb the long-range ferroelectric polar order to form the short–range PNRs, enhance the dielectric relaxor behavior, resulting in the high η. As a consequence, high W_{rec} of 3.29 J/cm^3 and ultrahigh η of 90.1% at the high external electric field of 310 kV/cm are achieved in $x = 0.5$ sample. These results reveal that the KNN-based ceramics are promising lead-free candidate for high-power electronic devices.

Acknowledgments

The work was supported by the National Natural Science Foundation of China (Grant No. 52072150), the Young Elite Scientists Sponsorship Program of the Chinese Academy of Space Technology (CAST) and Open Foundation of Guangdong Provincial Key Laboratory of Electronic Functional Materials and Devices (EFMD2021002Z).

References

[1] Y. Ming *et al.*, Orientation dependence of polarization-modulated photovoltaic effect of relaxor-based $Pb(In_{1/2}Nb_{1/2})O_3$–$Pb(Mg_{1/3}Nb_{2/3})O_3$–$PbTiO_3$ single crystals, *J. Alloy Compd.* **902**, 163777 (2022).
[2] F.-Z. Yao *et al.*, Multiscale structural engineering of dielectric ceramics for energy storage applications: From bulk to thin films, *Nanoscale* **12**, 17165 (2020).
[3] B. Fan *et al.*, Dielectric materials for high-temperature capacitors, *IET Nanodielectr.* **1**, 32 (2018).
[4] Y. Huan *et al.*, Intrinsic effects of ruddlesden-popper-based bifunctional catalysts for high-temperature oxygen reduction and evolution, *Adv. Energy Mater.* **9**, 1901573 (2019).
[5] Y. Huan *et al.*, Factors influencing Li^+ migration in garnet-type ceramic electrolytes, *J. Materiomics* **5**, 214 (2019).
[6] Z. Li *et al.*, Remarkably enhanced dielectric stability and energy storage properties in BNT-BST relaxor ceramics by A-site defect engineering for pulsed power applications, *J. Adv. Ceram.* **11**, 283 (2022).
[7] P. Lv *et al.*, Flexible all-inorganic Sm-doped PMN-PT film with ultrahigh piezoelectric coefficient for mechanical energy harvesting, motion sensing, and human-machine interaction, *Nano Energy* **97**, 107182 (2022).
[8] Z. Peiyao *et al.*, Perspectives and challenges for lead-free energy-storage multilayer ceramic capacitors, *J. Adv. Ceram.* **10**, 1153 (2021).
[9] D. Li *et al.*, Progress and perspectives in dielectric energy storage ceramics, *J. Adv. Ceram.* **10**, 675 (2021).
[10] Y. Huan *et al.*, Achieving ultrahigh energy storage efficiency in local-composition gradient-structured ferroelectric ceramics, *Chem. Eng. J.* **425**, 129506 (2021).
[11] H. Ji *et al.*, Ultrahigh energy density in short-range tilted NBT-based lead-free multilayer ceramic capacitors by nanodomain percolation, *Energy Storage Mater.* **38**, 113 (2021).
[12] X. Wang *et al.*, A combined optimization strategy for improvement of comprehensive energy storage performance in sodium niobate-based antiferroelectric ceramics, *ACS Appl. Mater. Inter.* **14**, 9330 (2022).
[13] H. Qi *et al.*, Ultrahigh energy-Sstorage density in $NaNbO_3$-based lead-free relaxor antiferroelectric ceramics with nanoscale domains, *Adv. Funct. Mater.* **29**, 1903877 (2019).
[14] W. Jia *et al.*, Advances in lead-free high-temperature dielectric materials for ceramic capacitor application, *IET Nanodielectr.* **1**, 3 (2018).
[15] T. Wu *et al.*, Influence of Sr/Ba ratio on the energy storage properties and dielectric relaxation behaviors of strontium barium titanate ceramics, *J. Mater. Sci. Mater. Electron.* **24**, 4105 (2013).
[16] G. Wang *et al.*, Electroceramics for high-energy density capacitors: Current status and future perspectives, *Chem. Rev.* **121**, 6124 (2021).
[17] Z. Lu *et al.*, Superior energy density through tailored dopant strategies in multilayer ceramic capacitors, *Energy Environ. Sci.* **13**, 2938 (2020).
[18] M. Zhang *et al.*, Significant increase in comprehensive energy storage performance of potassium sodium niobate-based ceramics via synergistic optimization strategy, *Energy Storage Mater.* **45**, 861 (2022).
[19] Y. Huan *et al.*, Achieving excellent energy storage reliability and endurance via mechanical performance optimization strategy in engineered ceramics with core-shell grain structure, *J. Materiomics* **8**, 601 (2022).
[20] H. Pan *et al.*, Ultrahigh energy storage in superparaelectric relaxor ferroelectrics, *Science* **374**, 100 (2021).
[21] M. Zhang *et al.*, Energy storage performance of $K_{0.5}Na_{0.5}NbO_3$-based ceramics modified by $Bi(Zn_{2/3}(Nb_{0.85}Ta_{0.15})_{1/3})O_3$, *Chem. Eng. J.* **425**, 131465 (2021).
[22] P.Y. Zhao *et al.*, Ultra-high energy storage performance in lead-free multilayer ceramic capacitors via a multiscale optimization strategy, *Energy Environ. Sci.* **13**, 4882 (2021).
[23] R.D. Shannon, Revised effective ionic radii and systematic studies of interatomic distances in halides and chalcogenides, *Acta Crystallographica Sec. A* **32**, 751 (1976).
[24] J.O. Gentner *et al.*, Dielectric losses in ferroelectric ceramics produced by domain-wall motion, *J. Appl. Phys.* **49**, 4485 (1978).
[25] M. Hoefling *et al.*, Optimizing the defect chemistry of $Na_{1/2}Bi_{1/2}TiO_3$-based materials: Paving the way for excellent high temperature capacitors, *J. Mater. Chem. C* **6**, 4769 (2018).
[26] F. Li *et al.*, Local structural heterogeneity and electromechanical responses of ferroelectrics: Learning from relaxor ferroelectrics, *Adv. Funct. Mater.* **28**, 1801504 (2018).
[27] G. Liu *et al.*, Ultrahigh dielectric breakdown strength and excellent energy storage performance in lead-free barium titanate-based relaxor ferroelectric ceramics via a combined strategy of composition modification, viscous polymer processing, and liquid-phase sintering, *Chem. Eng. J.* **398**, 125625 (2020).
[28] Y. Fan *et al.*, Enhanced thermal and cycling reliabilities in (K,Na)-$(Nb,Sb)O_3$-$CaZrO_3$-$(Bi,Na)HfO_3$ ceramics, *J. Adv. Ceram.* **9**, 349 (2020).
[29] X. Wang *et al.*, Optimizing the grain size and grain boundary morphology of $(K,Na)NbO_3$-based ceramics: Paving the way for ultrahigh energy storage capacitors, *J. Materiomics* **7**, 780 (2021).
[30] H. Borkar *et al.*, Anomalous change in leakage and displacement currents after electrical poling on lead-free ferroelectric ceramics, *Appl. Phys. Lett.* **107**, 122904 (2015).
[31] G. Wang *et al.*, Thermally-induced phase transformations in $Na_{0.5}Bi_{0.5}TiO_3$-$KNbO_3$ ceramics, *J. Am. Ceram. Soc.* **100**, 3293 (2017).
[32] M. Wang *et al.*, Ultrahigh energy storage density and efficiency in $Bi_{0.5}Na_{0.5}TiO_3$-based ceramics via the domain and bandgap engineering, *ACS Appl. Mater. Inter.* **14**, 19704 (2021).
[33] Z. Wang *et al.*, Reconfigurable quasi-nonvolatile memory/subthermionic FET functions in ferroelectric–2D semiconductor vdW architectures, *Adv. Mater.* **34**, 2200032 (2022).
[34] J. Lin *et al.*, Ultrahigh energy harvesting properties in temperature-insensitive eco-friendly high-performance KNN-based textured ceramics, *J. Mater. Chem. A* **10**, 7978 (2022).